Marine and Petroleum Geology 86 (2017) 526–536

Contents lists available at ScienceDirect

Marine and Petroleum Geology

journal homepage: www.elsevier.com/locate/marpetgeo

Research paper

Effects of oil expulsion and pressure on nanopore development in highly mature shale: Evidence from a pyrolysis study of the Eocene Maoming oil shale, south China

Yuke Liu [a, b], Yongqiang Xiong [a, *], Yun Li [a], Ping'an Peng [a]

[a] State Key Laboratory of Organic Geochemistry, Guangzhou Institute of Geochemistry, Chinese Academy of Sciences, Guangzhou 510640, China
[b] University of Chinese Academy of Sciences, Beijing 100049, China

ARTICLE INFO

Article history:
Received 18 January 2017
Received in revised form
9 June 2017
Accepted 9 June 2017
Available online 10 June 2017

Keywords:
Oil-shale
Anhydrous pyrolysis
Oil expulsion efficiency
Pressure
Nanopore evolution

ABSTRACT

The influence of oil-expulsion efficiency on nanopore development in highly mature shale was investigated by using anhydrous pyrolysis (425–600 °C) on solvent-extracted and non-extracted shales at a pressure of 50 MPa. Additional pyrolysis studies were conducted using non-extracted shales at pressures of 25 and 80 MPa to further characterize the impact of pressure on pore evolution at high maturity. The pore structures of the original shale and relevant artificially matured samples after pyrolysis were characterized by using low-pressure nitrogen and carbon-dioxide adsorption techniques, and gas yields during pyrolysis were measured. The results show that oil-expulsion efficiency can strongly influence gas generation and nanopore development in highly mature shales, as bitumen remained in shales with low oil expulsion efficiency significantly promotes gaseous hydrocarbon generation and nanopore (diameter < 10 nm) development. The evolution of micropores and fine mesopores at high maturity can be divided into two main stages: Stage I, corresponding to wet gas generation (EasyRo 1.2%–2.4%), and Stage II, corresponding to dry gas generation (EasyRo 2.4%–4.5%). For shales with low oil expulsion efficiency, nanopore (diameter < 10 nm) evolution increases rapidly in Stage I, whereas slowly in Stage II, and such difference between two stages may be attributed to the changes of the organic matter (OM)'s mechanical properties. Comparatively, for shales with high oil expulsion efficiency, the evolution grows slightly in Stage I, not as rapidly as shales with low efficiency, and decays in Stage II. The different pore evolution behaviors of these two types of shales are attributed to the contribution of bitumen. However, the evolution of medium–coarse mesopores and macropores (diameter >10 nm) remains flat at high maturation. In addition, high pressure can promote the development of micropores and fine mesopores in highly mature shales.

1. Introduction

There have been significant recent achievements in the exploration and development of shale gas in the lower Paleozoic marine shales of the Upper Yangtze region, south China (Chen et al., 2011; Sun et al., 2012; Tan et al., 2014; Zou et al., 2010). Industrial gas flows have been obtained from marine shales in the lower Cambrian Niutitang Formation and the lower Silurian Longmaxi Formation in the Sichuan Basin (Zou et al., 2015). Considering the burial depth and gas production yields, the Longmaxi Formation appears to be of high quality (Dong et al., 2015). However, in contrast to North American shales, marine shales in China are characterized by high thermal maturity (vitrinite reflectance, Ro = 2.0%–3.5%) and have experienced deep burial as well as multiple tectonic events (Xiao et al., 2013, 2015). Therefore, Chinese marine shales have unique properties regarding gas generation and pore development, including early oil-expulsion efficiency, late gas-generation ability, and pressure effects. An understanding of these properties could aid the evaluation and prediction of shale gas sweet spots in China.

Shale gas has biogenic and thermogenic origins. The source of thermogenic gas in shale consists of the cracking of kerogen, bitumen, and pyrobitumen (Jarvie et al., 2007). However, the relative contributions of these materials to shale gas vary greatly with increasing thermal maturity. Shale gas at low maturity is

* Corresponding author.
E-mail address: xiongyq@gig.ac.cn (Y. Xiong).

http://dx.doi.org/10.1016/j.marpetgeo.2017.06.012
0264-8172/

produced mainly from the primary cracking of kerogen. As maturation progresses, especially in the gas window, shale gas can also be derived from the secondary cracking of residual bitumen. The contribution of bitumen to gas generation is closely related to the oil expulsion efficiency at peak oil generation, meaning that relatively low oil expulsion efficiency at the oil window stage allows abundant bitumen to remain in the shales, which could enhance organic gas generation at high thermal maturity. Previous research has suggested that bitumen could become an important source of shale gas at high maturity (Xiong et al., 2016), and that gas production in highly mature shale would be reduced by 50% if the expulsion coefficient reaches 58% (Jia et al., 2014). Hao et al. (2013) suggested that the oil-expulsion efficiency at peak oil generation possibly led to the differences between the commercial values of shale gas exploration in the Niutitang shale and the Longmaxi shale. Both these black shales contain abundant pyrobitumen (Tian et al., 2015); however, the bitumen 'A' content in the Longmaxi Formation shales is higher than that in the Niutitang Formation (Tuo et al., 2016). Therefore, the higher gas content in lower Silurian shales may be explained by the lower oil-expulsion efficiency, when compared with the lower Cambrian shales.

For shales with low oil-expulsion efficiency, the remaining bitumen could not only enhance gas production, but also aid nanopore generation at high maturation, as demonstrated by the porous solid bitumen that has been observed in highly mature shales. For example, the bubble-like pores in quasi-solid bitumen in samples of the Marcellus, Barnett, and Posidonia shales at the gas window stage have been interpreted as evidence of pore formation after the secondary cracking of bitumen to gas at the gas window stage (Bernard et al., 2012a, 2012b; Milliken et al., 2013). Nanopores may develop more readily in solid bitumen (pyrobitumen) than in kerogen at the gas window. Porous organic matter in the Woodford Shale of maturity 1.4% Ro appears to be pyrobitumen, whereas nonporous organic matter is kerogen (Curtis et al., 2012). In addition, little porosity was observed in terrestrial maceral grains or vitrinites of the Haynesville shales (maturity of 2.42–2.58 VR_r) and the Bossier shales (1.79–2.26 VR_r), whereas high porosity (average up to 13.1%) occurs in solid bitumen (Klaver et al., 2015). Consequently, oil-expulsion efficiency may also significantly influence the differences in nanopore development between lower Cambrian and lower Silurian shales, as pores in the former are not as abundant as in the latter (Chen et al., 2011; Long et al., 2012). Porosity estimated in organic matters (defined as the ratio of organic pores to the volume of total organic matters) is about 10% for the lower Cambrian shales, which is far lower than that of the lower Silurian shales (36%) (Tian et al., 2015).

Unconventional shale gas systems are generally slightly to highly overpressured (Jarvie, 2012). In the Sichuan Basin, marine shale gas fields with commercial value in lower Paleozoic strata are typically overpressured (pressure coefficient = 1.3–2.1) (Zou et al., 2015). The lower Paleozoic strata in the Sichuan Basin experienced deep burial during the early Mesozoic, reaching a burial depth of 7–9 km by the end of the Early Cretaceous, followed by intense uplift from the late Mesozoic to the Cenozoic, resulting in 3–6 km of denudation (Liu et al., 2009; Ma et al., 2008; Zhang et al., 2008). This complicated tectonic evolution influenced the shale pressure system and strongly affected the generation, accumulation, and preservation of shale gas in this area. The burial history inferred from well W-117 in the Weiyuan area of the Sichuan Basin suggests that the maximum burial depths of Lower Cambrian and lower Silurian strata during the Early Cretaceous were 7 and 6 km, respectively (Xiao et al., 2012). Assuming a hydrostatic pressure increase of 10 MPa/km, the lower Paleozoic shales in the Sichuan Basin experienced a maximum hydrostatic pressure of around 60–70 MPa. Given the great variation in burial depths, it is possible that pressure affects gas generation and pore evolution in shales. Several works have investigated the role of pressure in hydrocarbon generation, but without consistent results. For example, some works report little or no significant pressure effect on hydrocarbon generation (Huang, 1996; Knauss et al., 1997), whereas others suggest that the yields of gaseous hydrocarbon at peak oil generation increase slightly with increasing pressure (Tao et al., 2010), and higher pressure could enhance the methane yield at high maturity (Shuai et al., 2006). Uguna et al. reported that gas yields are not affected by pressure up to 70 MPa, but are reduced slightly at 90 MPa (Uguna et al., 2014). Few studies have explored systematically the role of pressure on nanopore development in highly mature shales. The systems, closed or semi-closed, vary greatly with the different experimental techniques used to simulate pore evolution (Chen and Xiao, 2014; Sun et al., 2015). Different systems also involve different lithostatic and hydrostatic pressure conditions.

This paper aims to reveal the characteristics of nanopore development in highly mature shales and to evaluate the influences of oil expulsion and reservoir pressure on pore evolution at the highly mature stage by using confined anhydrous pyrolysis of artificially matured shale samples combined with solvent-extraction at set pressures.

2. Experiment

2.1. Samples

The oil shale considered here was collected from the Eocene Youganwo Formation at Maoming in Guangdong Province, southeast China. The sample is immature, with a Ro value of 0.5%. The organic geochemical parameters of this sample (labeled S_o) are presented in Table 1. The sample is organic-rich, with a total organic carbon (TOC) content of 16.83%. Rock-Eval analysis revealed this oil shale to have a T_{max} of 430 °C and a HI value of 716 mg/g TOC. The kerogen is type I–II. Minerals in the oil shale include mica (42.6%), quartz (21.2%), kaolinite (20.2%), montmorillonite (7.9%), pyrite (3%), dolomite (2.8%), and calcite (2.3%).

2.2. Pyrolysis experiment

2.2.1. Preparation of shale samples at the peak oil-generating stage

A semi-closed pyrolysis system was used to prepare samples at the peak of oil generation (Lu, 1990). First, crushed oil shale powder was loaded in a stainless steel cylinder (5 cm o.d. 3 cm i.d.) and sealed on both sides; it was then compacted by a jack under a vertical pressure of 50 MPa. The cylinder was heated in an oven at 370 °C for 24 h (equaling a Ro of 1.1%) (Fig. 1). After cooling, both seals were removed to collect the mature sample; however, some of the generated viscous oil adhered to the inner wall of the cylinder, resulting in an inevitable loss of OM. The loss ratio will be discussed later.

Prior to the following pyrolysis experiments, the artificially matured sample was separated into two parts. One part (labeled $S_{ex\text{-}370°C}$) was Soxhlet extracted with dichloromethane: methanol (93:7 v:v) for 72 h to remove the bitumen from the mature shale, representing shale with high oil-expulsion efficiency. The other non-extracted part ($S_{no\text{-}370°C}$) represents shale with low oil-expulsion efficiency. The TOC and Rock-Eval parameters of both samples are also listed in Table 1. The TOC content of $S_{no\text{-}370°C}$ is 7% less than that of S_o, which is a result of the unavoidable oil loss during pyrolysis. So the loss ratio of OM in $S_{no\text{-}370°C}$ due to simulation is 7%. And the TOC content of $S_{ex\text{-}370°C}$ is 40% of that of $S_{no\text{-}370°C}$, indicating that 60% of the organic matter in $S_{no\text{-}370°C}$ had been extracted as bitumen.

Table 1
Geochemical data of Maoming oil shale (S_o) and its two artificially mature products ($S_{no\text{-}370°C}$ and $S_{ex\text{-}370°C}$).

Sample	TOC (wt.%)	T_{max} (°C)	HI (mg/g TOC)	S1 (mg/g)	S2 (mg/g)	S3 (mg/g)
S_o	16.83	430	716	0.87	104.39	2.19
$S_{no\text{-}370°C}$	15.66	438	328	40.86	44.5	1.34
$S_{ex\text{-}370°C}$	6.29	445	164	0.16	10.73	1.89

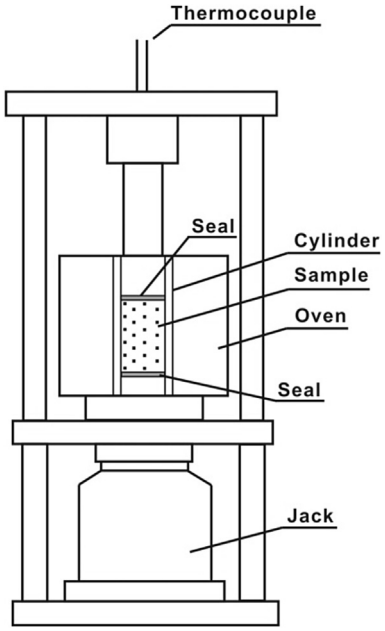

Fig. 1. High pressure, semi-closed pyrolysis system.

2.2.2. Confined anhydrous pyrolysis experiments

The pyrolysis experiments of $S_{no\text{-}370°C}$ and $S_{ex\text{-}370°C}$ were performed under anhydrous conditions in sealed gold tubes (6 mm o.d. 5.5 mm i.d. and 120 mm length). Details of the experiment have been described previously (Pan et al., 2012). Aliquots of the solid powder (0.4–1.0 g) were placed in the gold tubes. Each tube was flooded for 20 min with high-purity argon to expel air, then sealed, and loaded separately into stainless steel vessels.

Pyrolysis of $S_{ex\text{-}370°C}$ was performed at a constant pressure of 50 MPa and at temperatures of 425–600 °C with heating rates of 10 and 2 °C/h. For $S_{no\text{-}370°C}$, pyrolysis simulations were performed at three pressures (25, 50, and 80 MPa) from 425 to 600 °C, with heating rates of 10 and 2 °C/h. The deviations of pressure and temperature from the set values were less than 1 MPa and 1 °C, respectively. Individual stainless vessels were withdrawn from the oven at the set temperatures and rapidly cooled by quenching in water. The solid residues after the pyrolysis of $S_{ex\text{-}370°C}$ and $S_{no\text{-}370°C}$ are respectively called $S_{ex(M)}$ and $S_{no(M)}$, where M represents the thermal maturity of each sampling point.

2.3. Analyses

2.3.1. Gas composition analysis

Detailed procedures were reported previously (Pan et al., 2010). Briefly, the gold tube was loaded into a customized vacuum line connected to an Agilent 6890 N capillary gas chromatograph modified by Wasson ECE Instrumentation for determination of gas molecular composition. After the system was evacuated by a rotary pump, the gold tube was pierced to allow the gas flow into the vacuum line. A valve between the vacuum line and the GC instrument was used to introduce automatically a certain amount of gas into the GC system for measurements of molecular composition.

2.3.2. Pore structure characterization

Low-pressure nitrogen and carbon dioxide gas adsorption measurements were conducted on a Micromeritics ASAP-2460 Accelerated Surface Area and Porosimetry System. Samples were crushed to 60–120 mesh size and degassed at 110 °C for 12 h in a vacuum chamber prior to analysis to remove residual volatile material and free water. Nitrogen isotherms at 77 K were collected within a relative pressure (P/P_0) range of 0.005–0.998 (P is the balance pressure, and P_0 is the saturation pressure). Carbon dioxide isotherms were collected at 273.15 K at relative pressures of 0.00006–0.03.

The composited N_2 and CO_2 non-local-density functional theory (NLDFT) method is the most suitable approach for gas physisorption data analysis in shale pore-structure characterization (Wei et al., 2016). This method enables the most suitable detection range (0.33–100 nm) and has high reliability and accuracy. As the maximum pore diameter calculated by NLDFT is 100 nm, the NLDFT analysis based on N_2 and CO_2 composited adsorption isotherms is used here to investigate the characteristics of pores with diameters (D) up to 50 nm. Barrett–Joyner–Halenda (BJH) theory using the adsorption branch of the nitrogen isotherms is applied to characterize macropores (D > 50 nm); the theory is based on the Kelvin equation assuming cylindrical pores, corrected for multilayer adsorption (Barrett et al., 2014). Pore size distributions (PSDs) were obtained by using DFT methods based on adsorption isotherms.

3. Results and discussion

3.1. Gas generation

To evaluate the thermal maturity of shales during pyrolysis, the EasyRo% values suggested by Sweeney and Burnham (1990) are used here. The calculated results show that the corresponding thermal maturity during the whole pyrolysis process ranges from EasyRo 1.22%–4.07% with a heating rate of 10 °C/h, and from EasyRo 1.56%–4.45% with a heating rate of 2 °C/h (Table 2), which approximately covers the whole gas window stage. Fig. 2 shows the cumulative yields of methane and C_2–C_5 gaseous hydrocarbons during the artificial maturation of $S_{ex(M)}$ and $S_{no(M)}$.

Table 2
EasyRo% calculated at different temperatures at two heating rates.

Temperature (°C)	Easy Ro (%)	
	10 °C/h	2 °C/h
425	1.22	1.56
450	1.57	1.97
475	1.94	2.42
500	2.35	2.91
525	2.81	3.41
550	3.28	3.84
575	3.73	4.18
600	4.07	4.45

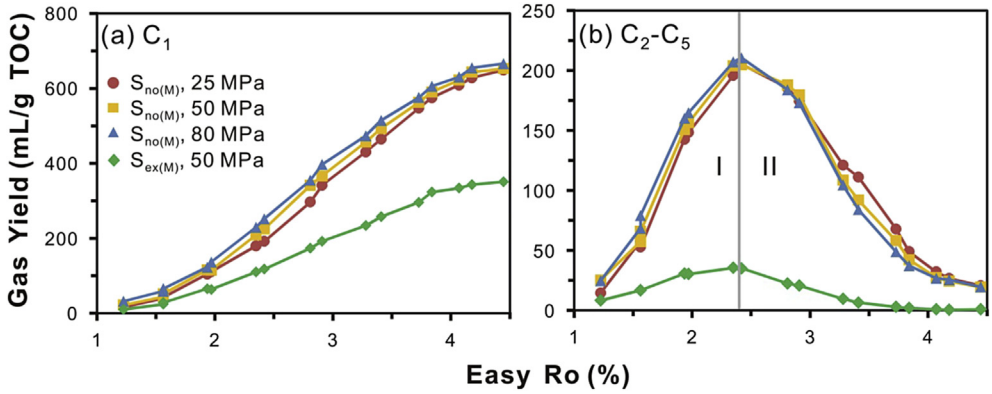

Fig. 2. The yields of methane (a) and C_2–C_5 (b) of $S_{no(M)}$ at pressures of 25, 50 and 80 MPa, and $S_{ex(M)}$ at pressure of 50 MPa, as functions of thermal maturity indicated by EasyRo%.

3.1.1. Effect of oil expulsion on gas generation

The results of pyrolysis of $S_{no(M)}$ and $S_{ex(M)}$ at 50 MPa are used to illustrate the effect of oil expulsion on gas generation. The variation in the yields of the C_2–C_5 gaseous hydrocarbons (Fig. 2b) indicates two main stages during gas generation: wet gas generation (Stage I) and dry gas generation (Stage II). Stage I, corresponding to EasyRo 1.22%–2.40%, is characterized by the formation of C_2–C_5 gaseous hydrocarbons. When EasyRo >2.40%, the decomposition rate of C_2–C_5 gaseous hydrocarbons exceeds their generation rate, indicating the evolution of gas generation entering Stage II.

Fig. 2 shows that the gas yields of $S_{ex(M)}$ are much lower than those of $S_{no(M)}$. The yields of methane and C_2–C_5 gaseous hydrocarbons generated by $S_{no(2.42\%)}$ are respectively about two times and six times those generated by $S_{ex(2.42\%)}$, indicating that bitumen remaining in shales with low oil expulsion is a major contributor to gas generation at the highly mature stage. The extracted shales lose most of their gas generation potential at the thermal maturity stage of EasyRo >1.22%, owing to the removal of bitumen. The proportion of gaseous hydrocarbon attributed to bitumen in $S_{no(M)}$ at different maturations ($B_{(M)}$) can be calculated as follows:

$$B_{(M)} = \left(Y_{no(M)} - Y_{ex(M)}\right) \Big/ Y_{no(M)} \times 100\%, \quad (1)$$

where $Y_{no(M)}$ and $Y_{ex(M)}$ respectively refer to the measured gas yields (mL/g TOC) of $S_{no(M)}$ and $S_{ex(M)}$ at the corresponding maturation (M = 1.22%–4.45%). $Y_{no(M)}$ includes the amounts of kerogen-cracking gas and bitumen-cracking gas in $S_{no(M)}$, and $Y_{ex(M)}$ is the amount of kerogen-cracking gas in $S_{ex(M)}$. The values of $B_{(M)}$ for methane and C_2–C_5 yields are 43%–53% and 70%–98%, respectively. Quantitative analyses of solvent extraction and TOC show that bitumen produced at the peak oil-generation stage accounts for 60% of the TOC in the non-extracted shale. Such reserved bitumen contributes 43%–53% of the methane yield and 70%–98% of the C_2–C_5 gas yield at high maturation. This result indicates that bitumen reserved in shales with low hydrocarbon expulsion efficiency has a strong capacity for gas generation at the high maturity stage, which is consistent with previous findings (Jia et al., 2014; Xiong et al., 2016).

3.1.2. Effect of pressure on gas generation

Comparison of the yields of methane and C_2–C_5 gaseous hydrocarbons generated at 25, 50, and 80 MPa (Fig. 2) shows that higher pressure can slightly promote methane generation at high maturity, as the yields of methane increase with increasing pressure (Fig. 2a), consistent with the results of a previous study (Shuai et al., 2006). The C_2–C_5 gaseous hydrocarbons display the same trend in Stage I (i.e., EasyRo 1.22%–2.40%), suggesting that higher pressure may slightly enhance the generation of C_2–C_5 gaseous hydrocarbons. However, higher pressure can also accelerate the decomposition of C_2–C_5 gaseous hydrocarbons in Stage II (Fig. 2b). Overall, this effect of pressure on the formation of methane and C_2–C_5 gaseous hydrocarbons is relatively small.

3.2. Nanopore structure

The pore structures of S_o, $S_{no\text{-}370°C}$, $S_{ex\text{-}370°C}$, and their pyrolytic residues ($S_{no(M)}$ and $S_{ex(M)}$) were characterized using low-pressure N_2 and CO_2 adsorption methods. To better understand their structural evolution, nanopores were subdivided into micropores (D < 2 nm), fine mesopores (2 < D < 10 nm), medium mesopores (10 < D < 25 nm), coarse mesopores (25 < D < 50 nm), and macropores (D > 50 nm), according to the IUPAC classification (Thommes et al., 2015) and previous work (Chalmers et al., 2012). The PSDs of the original shale sample (S_o) and the extracted ($S_{ex\text{-}370°C}$) and non-extracted ($S_{no\text{-}370°C}$) shales are presented in Fig. 3. The original shale sample exhibits a bimodal PSD, with the dominant pores being micropores and mesopores. $S_{no(M)}$ and $S_{ex(M)}$ pyrolyzed at 10 °C/h were selected to characterize the PSD variances during simulation (Fig. 4), as discussed below.

3.2.1. Adsorption isotherms

Typical nitrogen isotherms for the pyrolytic residues (i.e., $S_{no(4.07\%)}$ and $S_{ex(4.07\%)}$, heated to 600 °C at 10 °C/h, 50 MPa) are shown in Fig. 5a and b, which correspond to a composite of Types II

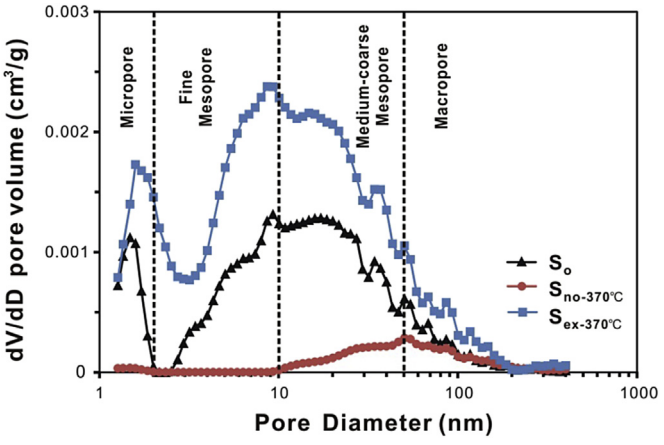

Fig. 3. Plot of dV/dD versus D for the pore size distribution of S_o, $S_{no\text{-}370°C}$ and $S_{ex\text{-}370°C}$, obtained by the DFT method based on N_2 adsorption isotherms.

method based on N_2 adsorption isotherms.

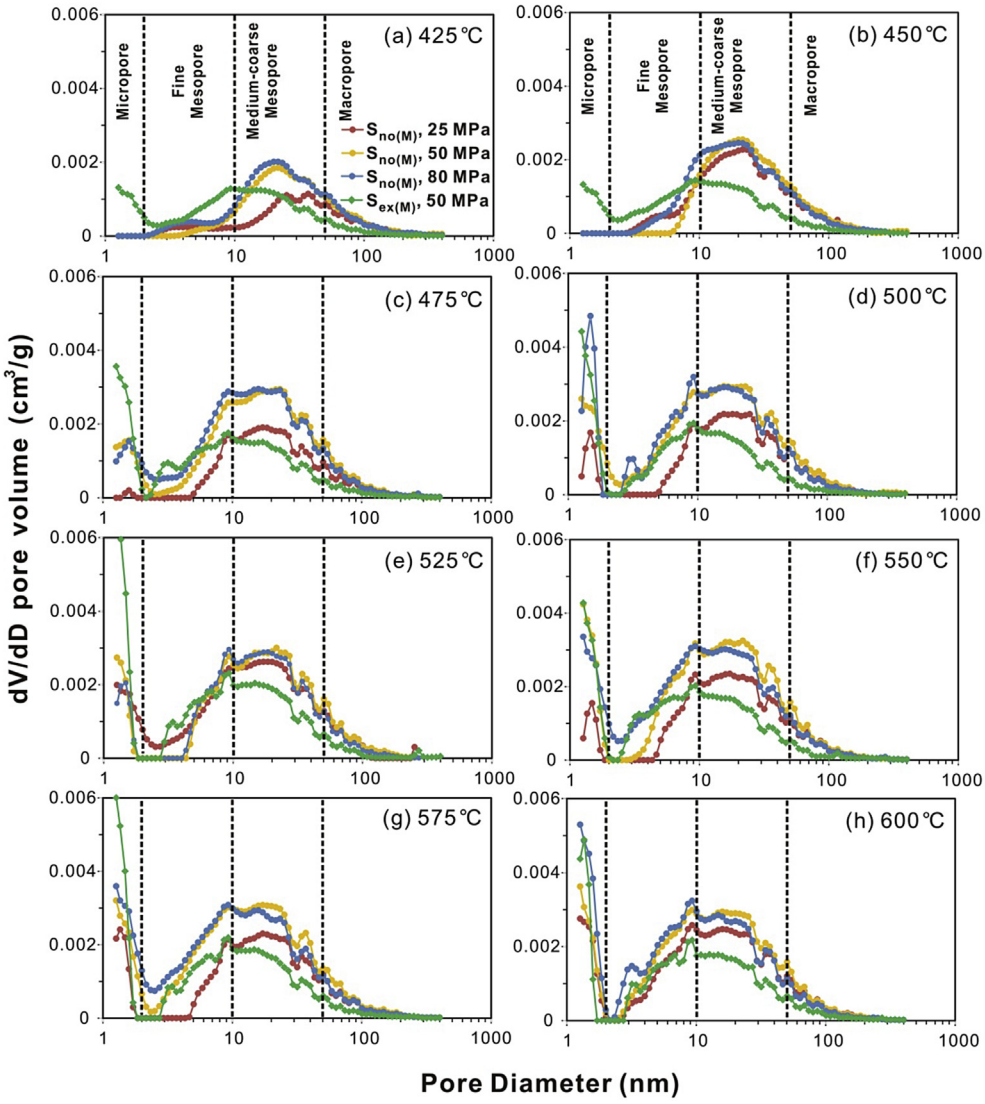

Fig. 4. Plot of dV/dD versus D for the pore size distribution of $S_{no(M)}$ pyrolyzed at pressures of 25, 50 and 80 MPa, and $S_{ex(M)}$ at pressure of 50 MPa, from 425 °C to 600 °C, at 10 °C/h (a–h), obtained by the DFT method based on N_2 adsorption isotherms.

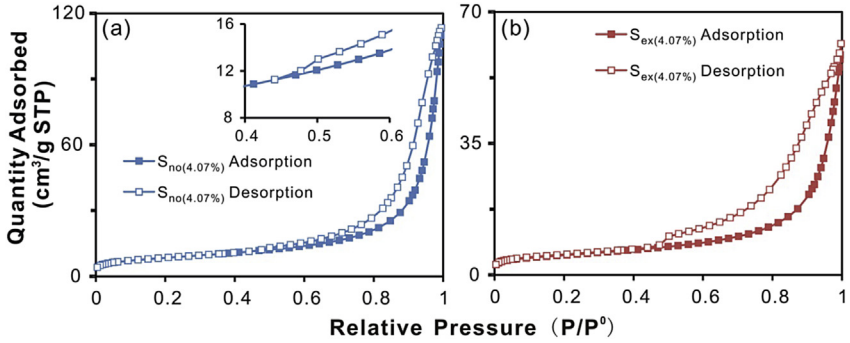

Fig. 5. N_2 isotherms of $S_{no(4.07\%)}$ (a) and $S_{ex(4.07\%)}$ (b).

and IV, as defined by IUPAC (Thommes et al., 2015). The isotherms, close to Type II, increase without limit when $P/P^0 = 1$, which is an indicator of macropores. The Type IV isotherm is characterized by a hysteresis loop that is associated with capillary condensation in the mesopores structure. The loop is close to type H2 (a), indicating material composed of ink-bottle pores with narrow necks (Thommes et al., 2015). Fig. 6 gives an overview of the carbon dioxide isotherms of $S_{no(M)}$ pyrolyzed at 50 MPa and 10 °C/h, which

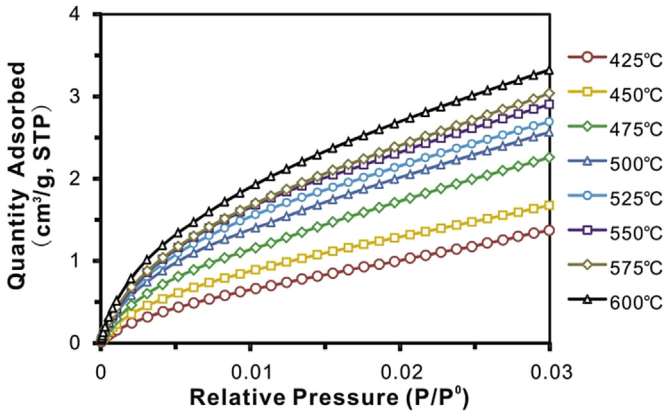

Fig. 6. CO_2 isotherms of $S_{no(M)}$ pyrolyzed at 50 MPa at 10 °C/h.

corresponds to a Type I isotherm given by microporous solids (Thommes et al., 2015). The quantity adsorbed at P/P^0 of 0.03 for $S_{no(M)}$ increases with rising temperature. Generally, the N_2 and CO_2 isotherms indicate that these shales possess complex pore structures, with the pore sizes ranging from micropores to macropores.

3.2.2. Effect of thermal maturity on nanopore structure

Variations in the pore structure characteristics of $S_{no\text{-}370°C}$ and $S_{no(M)}$ pyrolyzed at 50 MPa at varying thermal maturations are used to illustrate the effect of thermal maturity on pore evolution.

Unlike S_o, $S_{no\text{-}370°C}$ shows a unimodal PSD with a peak at 50 nm (Fig. 3). $S_{no(M)}$ pyrolyzed at 425 and 450 °C has a PSD with a broad peak within medium–coarse mesopores (Fig. 4a and b). However, when the temperature rises from 475 to 600 °C, a new peak appears at the micropore range and the value of dV/dD shows a bump at D = 9 nm, resulting in a bimodal PSD (Fig. 4c–h).

Pore volumes and specific surface areas of the different pore size types for S_o, $S_{no\text{-}370°C}$, and $S_{no(M)}$ at a range of maturities are presented in Fig. 7. Compared with the original shale sample (S_o), $S_{no\text{-}370°C}$ at the peak of oil generation has a much lower pore volume and specific surface area (Fig. 7a–h), indicating that the generated bitumen at the oil window stage could fill or block the nanopores in the shales. This result is consistent with the findings of Valenza et al. (2013). During the subsequent thermal pyrolysis in confined gold tubes, two stages are identified in the evolution of micropores and fine mesopores in $S_{no(M)}$. Pores grew rapidly in Stage I (from EasyRo 1.22%–2.40%), which corresponds to a wet gas stage, and grew slowly in Stage II (from EasyRo 2.40%–4.45%), corresponding to a dry gas stage (Fig. 7a–d). At the highest maturity stage (EasyRo 4.45%), the pore volume and surface area of micropores in $S_{no(4.45\%)}$ are respectively 5 times and 3.5 times those in S_o (Fig. 7a and b). Similarly, for fine mesopores, the pore volume and surface area in $S_{no(4.45\%)}$ are respectively 3.7 times and 4.3 times those in S_o (Fig. 7c and d).

In contrast to the continuous changes in the values of micropore and fine mesopore parameters between $S_{no\text{-}370°C}$ and $S_{no(1.22\%)}$, the pore parameters of medium–coarse mesopores and macropores in $S_{no(1.22\%)}$ show an abrupt increase compared with those of $S_{no\text{-}370°C}$ (Fig. 7e–h). As pyrolysis from 425 to 600 °C only covers the main gas stage, pore evolution during the late oil window and early gas window was not simulated, thus resulting in the discontinuity. Then, during the following thermal simulation from EasyRo 1.2%–4.5%, the evolution of medium–coarse mesopores and macropores remains almost steady, showing only a slight increase in medium–coarse mesopores from EasyRo 1.2%–2.0%.

Abundant micropores occur in OM in highly mature shales (Loucks et al., 2009), and OM content is positively correlated with micropore volume in shales (Chalmers and Bustin, 2007; Ross and Marc Bustin, 2009; Yang et al., 2014, 2016). Maturity also significantly enhances the development of micropores and mesopores in organic-rich shales, as these pores increase when maturation progresses from the oil window to the gas window (Chen and Xiao, 2014). Therefore, the development of micropores and fine mesopores in this study is closely related to OM, and the generation of micropores and fine mesopores (D < 10 nm) at high maturity probably resulted from the secondary cracking of bitumen to gas (Mastalerz et al., 2013). In contrast, mesopores and macropores in shales are closely associated with minerals rather than OM (Hua, 2012; Yang et al., 2014, 2016). The relation between mineral-associated macropores and maturity is relatively weak (Chao et al., 2013; Tang et al., 2015), or possibly the pores in the mineral matrix have a complicated response to thermal maturation (Curtis et al., 2012; Ghanizadeh et al., 2014). Therefore, the evolution of medium–coarse mesopores and macropores appears to be flat at high maturity.

The relatively slow rate of increase in micropore and fine mesopore evolution during Stage II (compared with Stage I) may be attributed to changes in the mechanical properties of OM (Emmanuel et al., 2016; Fitzgerald, 1956; Wang et al., 2014; Yang et al., 2016). In Stage I, after an initial softening, the OM with aliphatic C-H bonds behaves as a viscous fluid and cracks during plastic deformation. During this period, organic gas is generated and stored within OM, resulting in the formation of nanopores. However, when the maturity progresses to Stage II, the carbonization of OM means that it solidifies into brittle semi-coke or coke. Thus, the cracking of coke leads to the destruction, merging, and collapse of OM-hosted pores, and the gas generated can no longer be stored in situ.

3.2.3. Effect of oil expulsion on nanopore structure

Unlike $S_{no\text{-}370°C}$, $S_{ex\text{-}370°C}$ shows a similar PSD to that of S_o, being unimodal with dominant micropores and mesopores (Fig. 3). During the subsequent pyrolysis, no obvious variance arises in the modalities of the PSDs of $S_{ex(M)}$ at different temperatures; only a higher peak in the micropore range emerges with increasing maturity (Fig. 4a–h). Compared with $S_{no(M)}$, the PSD of $S_{ex(M)}$ exhibits a lower peak in the mesopore range and a higher peak in the micropore range.

Fig. 7 shows the pore volumes and specific surface areas for the different pore size types of $S_{ex\text{-}370°C}$ and $S_{ex(M)}$ at a range of maturities. The solvent extraction appears to have released pores that were previously filled or blocked by bitumen. For example, $S_{ex\text{-}370°C}$ shows a large increase in micro-to macropores when compared with $S_{no\text{-}370°C}$, which is consistent with previous research (Mastalerz et al., 2013; Valenza et al., 2013).

Unlike the continuous changes in the micropore parameters of $S_{ex\text{-}370°C}$ and $S_{ex(1.22\%)}$ (Fig. 7a and b), there is a sharp decrease in the mesopore and macropore parameters of $S_{ex(1.22\%)}$ when compared with $S_{ex\text{-}370°C}$ (Fig. 7c–h). This may be attributed to compaction resulting from pressure. As nanopores in $S_{ex\text{-}370°C}$ contain largely artificially produced inorganic pores and organic (kerogen) pores, which were once clogged by soluble bitumen, the applied pressure of 50 MPa during pyrolysis in the confined gold tubes may have led to the compaction of mesopores and macropores in $S_{ex(M)}$. This was possibly due to the loss of internal support provided by OM. Mineral-hosted pores, regarded as the primary contributor to macropores at the gas window, are commonly observed at the organic–inorganic interface (Mathia et al., 2016), and mesopores within clay aggregates are commonly filled with OM (Shi et al., 2015). The finely dispersed OM within an inorganic matrix allows mesopores and macropores to survive compaction (Shi et al., 2015).

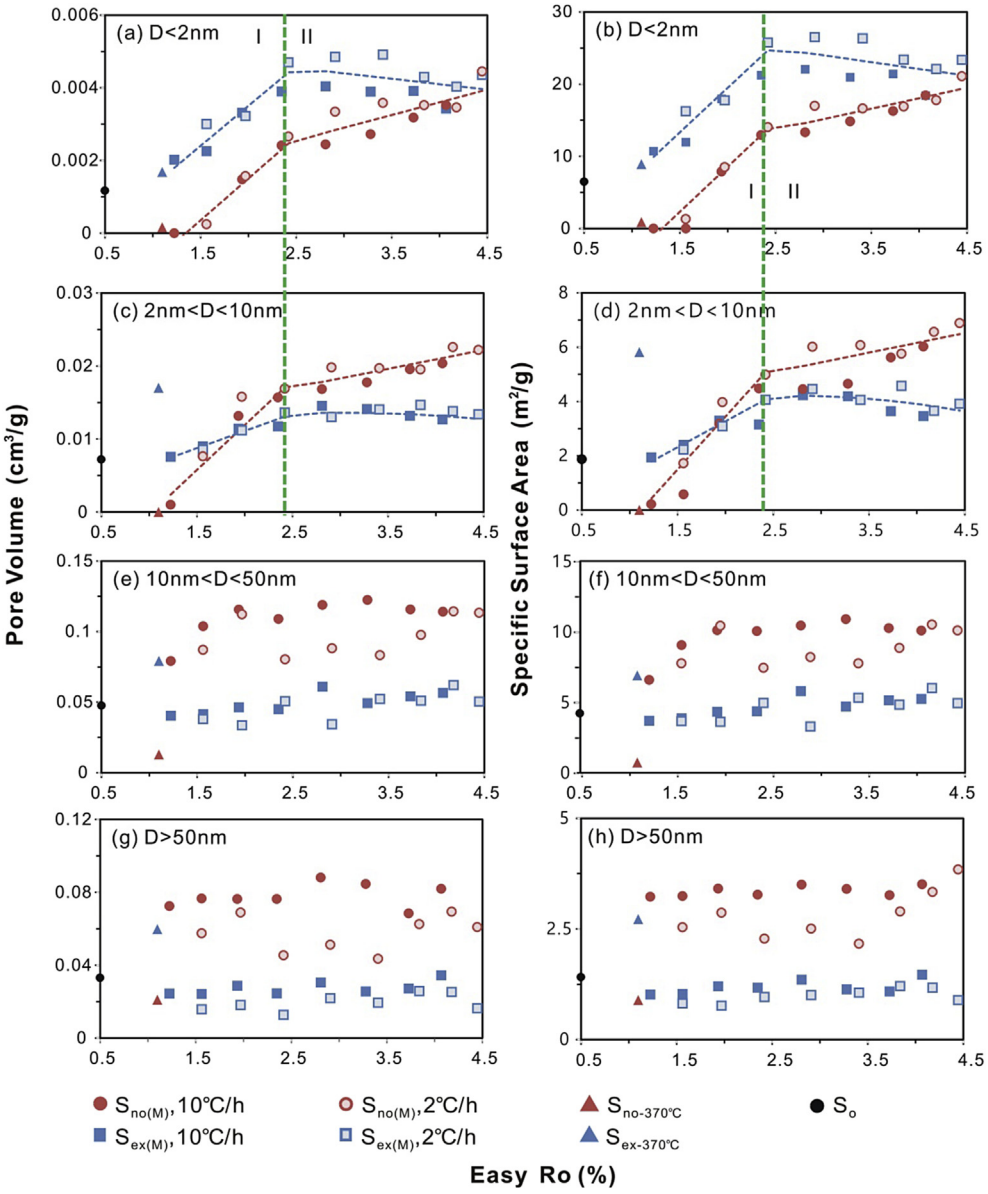

Fig. 7. Pore volumes and specific surface areas of micropores (a and b), fine mesopores (c and d), medium-coarse mesopores (e and f) and macropores (g and h) in S_o, $S_{no\text{-}370°C}$, $S_{ex\text{-}370°C}$, $S_{no(M)}$ and $S_{ex(M)}$, as functions of thermal maturity indicated by EasyRo%. The black dot represents parameters of S_o. Pore parameters of $S_{no\text{-}370°C}$ and $S_{ex\text{-}370°C}$ are presented with triangles. The pyrolytic residues in gold tube system at 10 °C/h and 2 °C/h are drawn as solid and hollow dots, respectively. Dotted lines represent fitting curves of pore parameters. There is a close relationship between pore parameters and maturation in Stage I (variance (R^2) > 0.9), and a moderate relationship in Stage II.

Thus, without inner support from OM, inorganic-associated mesopores and macropores in $S_{ex(M)}$ would have been strongly compacted by pressure, whereas compaction has, in reality, less effect on micropores.

As discussed above, during the thermal pyrolysis from EasyRo 1.22%–4.45%, the micropores and fine mesopores in the $S_{no(M)}$ series shows a rapid increase in Stage I and a slight increase in Stage II. In contrast, the evolution of the $S_{ex(M)}$ series showed initial growth in Stage I and a slight decrease in Stage II (Fig. 7a–d). The gap between the micropores parameters of $S_{no(M)}$ and $S_{ex(M)}$ narrows with increasing maturation, as these two suites are almost identical at EasyRo 4.45% (Fig. 7a and b). As for the evolution of fine mesopores, such pores in $S_{no(M)}$ exceed those in $S_{ex(M)}$ above EasyRo 2.0%, and the gap between $S_{no(M)}$ and $S_{ex(M)}$ gradually widens until EasyRo 4.45% (Fig. 7c and d).

The evolution of medium–coarse mesopores and macropores in both $S_{no(M)}$ and $S_{ex(M)}$ shows flat trends with increasing maturation, with the pore parameters being lower in $S_{ex(M)}$ than in $S_{no(M)}$ (Fig. 7e–h). This result may be attributed to the effect of pressure, as pores in $S_{ex(M)}$ are strongly compacted without support from OM.

The thermal simulation of $S_{ex(M)}$ from EasyRo 1.22%–4.45% shows that it has inherited the pores artificially produced by Soxhlet extraction. Therefore, in order to eliminate the interference of Soxhlet extraction and compaction on pore structure, the values of pore volume and specific surface area (for D < 10 nm) in $S_{ex(M)}$ and $S_{no(M)}$ at EasyRo 1.56%–4.45% are corrected by subtracting the corresponding values of $S_{ex(1.22\%)}$ and $S_{no(1.22\%)}$, respectively. Fig. 8a and b shows that the corrected micropore parameters of $S_{ex(M)}$ and $S_{no(M)}$ are identical in Stage I, both exhibiting sharply increasing trends. However, the evolutions differ in Stage II, as $S_{no(M)}$ shows a continuously increasing trend, but not as fast as that in Stage I. $S_{ex(M)}$ decays gradually until EasyRo 4.45%. The values of the

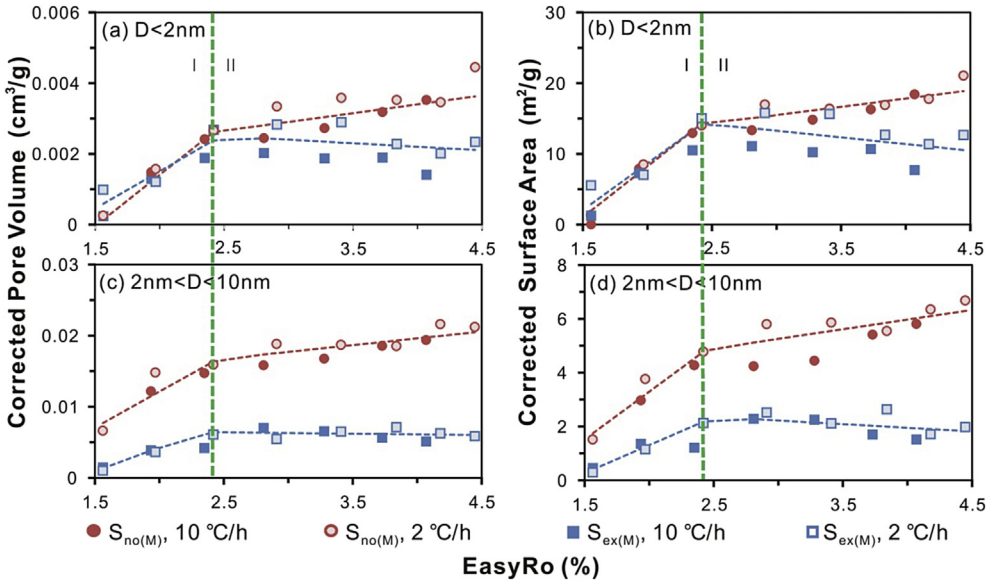

Fig. 8. Corrected pore volumes and surface area of micropore (a and b) and fine mesopore (c and d) in $S_{no(M)}$ and $S_{ex(M)}$ at 50 MPa. Dotted lines represent the fitting curves of pore parameters. There is a close relationship between pore parameters and maturation in Stage I ($R^2 > 0.8$), and a moderate relationship in Stage II.

micropore parameters of $S_{no(4.45\%)}$ are nearly twice as much as those of $S_{ex(4.45\%)}$. These observations indicate that bitumen reserved in the shales has little effect on micropore evolution at the wet gas stage, whereas it plays an important role in accelerating micropore development in the dry gas stage. The corrected fine mesopore parameters (Fig. 8c and d) increase in both $S_{no(M)}$ and $S_{ex(M)}$ during Stage I, with $S_{no(M)}$ growing faster than $S_{ex(M)}$. With further maturation in Stage II, the growth rate of $S_{no(M)}$ slows down. However, unlike the monotonically increasing trend of $S_{no(M)}$, the evolution of $S_{ex(M)}$ flattens or decays slightly in Stage II, resulting in an increasing gap between these two suites, as the values of pore parameters of $S_{no(4.45\%)}$ are around three times those of $S_{ex(4.45\%)}$.

Such decreasing trends of micropores and fine mesopores in $S_{ex(M)}$ during the dry gas stage may result from its relatively low OM content, as these pores are thought to develop primarily in OM (Hua, 2012; Yang et al., 2016). Compared with $S_{no(M)}$, $S_{ex(M)}$ has a lower TOC and higher mineral content. Therefore, its nanopore structure may be more sensitive to changes in clay minerals compared with $S_{no(M)}$. Diagenesis of clay minerals mainly involves dehydration and microstructural changes, resulting in reduced porosity (Neaman et al., 2003; Noyan et al., 2006). Therefore, the decaying trend exhibited by $S_{ex(M)}$ during the dry gas stage may be ascribed to (1) less bitumen (or lower TOC), as the evolution of micropores and fine mesopores is controlled mainly by OM (Chalmers and Bustin, 2007; Ross and Marc Bustin, 2009; Yang et al., 2016); and (2) the dehydration/framework collapse of clay minerals (Neaman et al., 2003; Noyan et al., 2006).

The gap between the micropore and fine mesopore (D < 10 nm) volumes of $S_{no(M)}$ and $S_{ex(M)}$ is considered to reflect the contribution of bitumen. To quantify the contribution of bitumen to pore evolution, the proportion of pore (D < 10 nm) volume attributed to bitumen in $S_{no(M)}$ ($B'_{(M)}$) at maturation from EasyRo 1.56%–4.45% was calculated as follows:

$$B'_{(M)} = \left(\left(V_{no(M)} - V_{no(1.22\%)}\right) - \left(V_{ex(M)} - V_{ex(1.22\%)}\right)\right) \Big/ \left(V_{no(M)} - V_{no(1.22\%)}\right) \times 100\%, \quad (2)$$

where $V_{no(M)}$, $V_{ex(M)}$, $V_{no(1.22\%)}$, and $V_{ex(1.22\%)}$ are the pore (<10 nm) volumes (cm^3/g) of $S_{no(M)}$ (M = 1.56%–4.45%), $S_{ex(M)}$ (M = 1.56%–4.45%), $S_{no(1.22\%)}$, and $S_{ex(1.22\%)}$, respectively. The calculated values of $B'_{(M)}$ range from 52% to 72% during thermal simulation. This indicates that bitumen produced at the peak oil generation stage, accounting for 60% of TOC in non-extracted shale, contributes 52%–72% of the pore (D < 10 nm) volume in highly mature shale.

To evaluate the relationship between nanopore development and OM, the corrected pore volume and surface area of $S_{no(M)}$ and $S_{ex(M)}$ are normalized as divided by the TOC contents of $S_{no\text{-}370°C}$ and $S_{ex\text{-}370°C}$, respectively, (Fig. 9). The micropore parameters of $S_{ex(M)}$ are higher than those of $S_{no(M)}$ (Fig. 9a and b), as the presence of bitumen acts to reduce the volume of micropores. However, no obvious differences are observed between the fine mesopores of these two suites of samples (Fig. 9c and d). This indicates that despite the capacity of bitumen for pore generation, its presence may also fill the intra- and intergranular spaces among kerogen and minerals (Bernard et al., 2012a, 2012b). In terms of micropores, pore blocking by bitumen outweighs its pore generation effect, resulting in a reduction in micropore volume in $S_{no(M)}$ relative to $S_{ex(M)}$. However, these two effects on fine mesopores may counteract each other, as no apparent differences arise between $S_{no(M)}$ and $S_{ex(M)}$.

3.2.4. Effect of pressure on nanopore structure

The PSDs of $S_{no(M)}$ at pressures of 25, 50, and 80 MPa exhibit similar modalities, being unimodal at 425 and 450 °C, and bimodal at higher temperatures (Fig. 4a–h). However, the peak heights within the mesopore range at 25 MPa are lower than those at 50 and 80 MPa at each temperature. The diameters at which the maximum dV/dD arises are similar for the different pressures at each temperature, except for at 425 °C, for which the diameter at 25 MPa is lower than those at 50 or 80 MPa (Fig. 4a).

Nanopores are classified into three types here: micropores and fine mesopores (<10 nm), medium–coarse mesopores (10–50 nm), and macropores (>50 nm). The variations in pore volume and specific surface area of micropores and fine mesopores with thermal maturity at pressures of 25, 50, and 80 MPa are shown in Fig. 10a and b. Overall, pore evolutions at different pressures show similar trends; i.e., pore parameters exhibit rapid growth in Stage I and relatively slow growth in Stage II. Increasing the pressure also promotes the development of micropores and fine mesopores

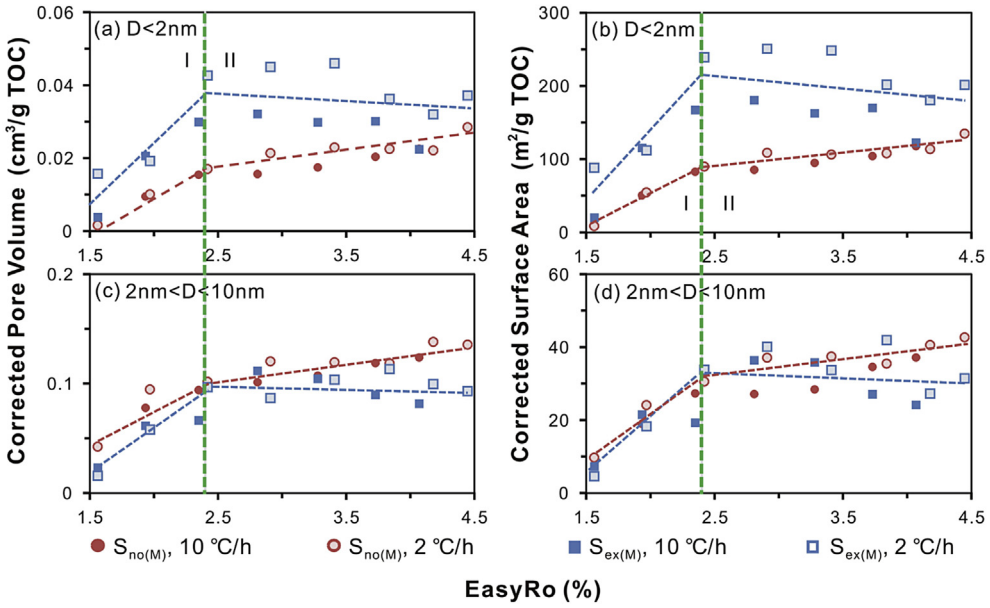

Fig. 9. TOC normalized corrected pore volumes and surface area of micropore (a and b) and fine mesopore (c and d) in $S_{no(M)}$ and $S_{ex(M)}$ at 50 MPa. Dotted lines represent the fitting curves of pore parameters. There is a close relationship between pore parameters and maturation in Stage I ($R^2 > 0.8$), and a moderate relationship in Stage II.

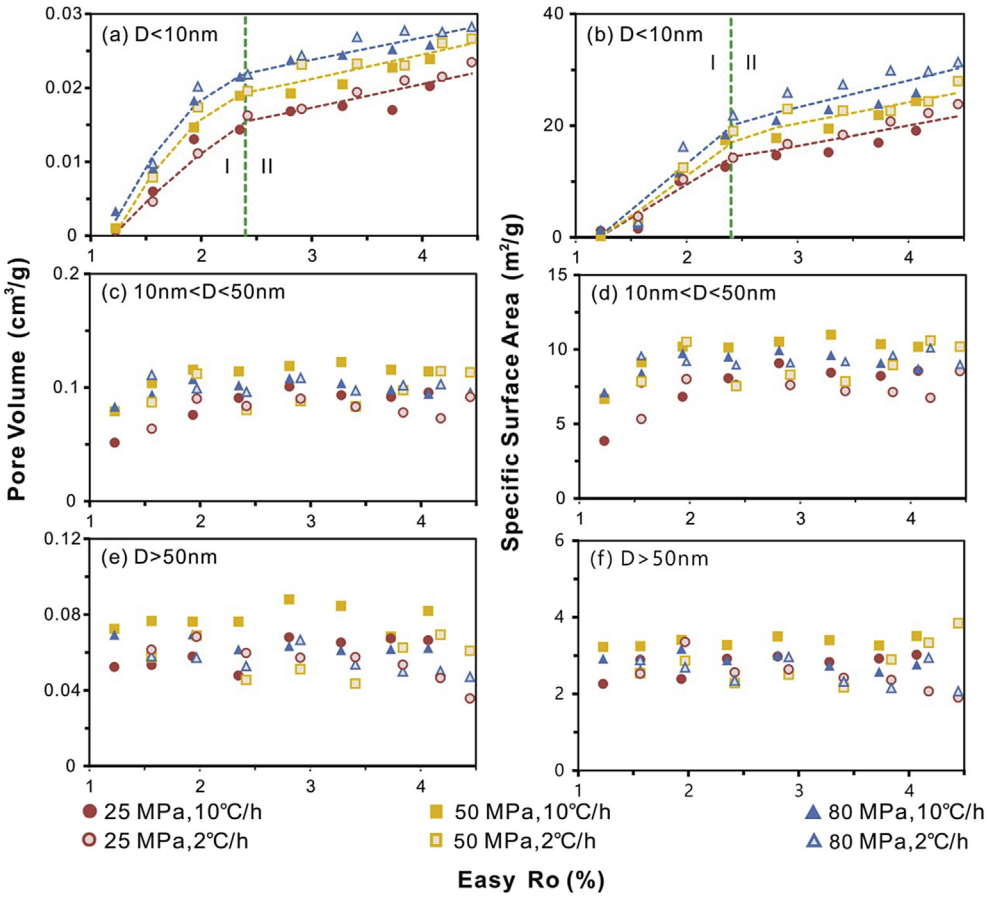

Fig. 10. Pore volumes and specific surface areas of micropores and fine mesopores (a and b), medium-coarse mesopores (c and d) and macropores (e and f) in $S_{no(M)}$ pyrolyzed at pressures of 25, 50 and 80 MPa. Dotted lines represent fitting curves of pore parameters with $R^2 > 0.9$ in Stage I and $R^2 > 0.7$ in Stage.

(D < 10 nm), as the pore parameters increase when pressure rises from 25 to 80 MPa at each maturity. The evolutions of medium–coarse mesopores and macropores are similar at different pressures (Fig. 10c–f), indicating that pressure has no remarkable effect on such pore evolution.

The results discussed above indicate that high pressure can

notably promote the generation of micropores and fine mesopores in highly mature shales, but that it has little impact on the development of medium–coarse mesopores and macropores. Overall, pressure affects nanopore evolution in two main ways: compaction and maintenance. Pores may be strongly compacted when the external pressure exceeds the pore pressure. However, with increasing burial depth and maturity, the cracking of OM in a closed reservoir increases the pore pressure, which may counteract the effect of external pressure, thereby allowing the newly generated pores to be maintained. In this view, high external pressure favors nanopore generation as it balances the internal pore pressure. The interaction between pressures inside and outside of pores controls the generation and preservation of nanopores. However, in order to model the relationship between pressure and pore generation, further comparison using different experimental apparatuses with variable lithostatic and hydrostatic pressures is needed.

Assuming a hydrostatic pressure gradient of 10 MPa/km, the pressures set in the pyrolysis simulation of this study (25, 50, and 80 MPa) are equivalent to depths of 2.5, 5, and 8 km, respectively, which correspond to the history of increasing burial depth of lower Paleozoic marine shales in the Sichuan Basin. According to previous models, absorbed gas in the lower Paleozoic marine shales first increases with burial depth and then reaches a peak at ~10 MPa under hydrostatic conditions; it then decreases with further burial (Hao et al., 2013). The estimated amount of free gas increases monotonically with burial depth (or hydrostatic pressure), and a higher pressure coefficient favors the preservation of free gas (Xiao et al., 2015). Micropores in shales are considered to be the main stores of absorbed gas, and free gas is stored mainly in meso- and macropores. Thus, simply considering the effect of pressure, we suppose that pores (D < 10 nm) in Lower Cambrian and lower Silurian shales may have developed continuously with increasing burial depth from the start of sedimentation to the Early Cretaceous, while providing increasing storage for shale gas when hydrostatic pressure increased from 25 to 80 MPa.

4. Conclusions

Anhydrous pyrolysis experiments simulating high maturity on two suites of artificially mature solvent-extracted and non-extracted shale samples were conducted. Pore characteristics were investigated by low-pressure nitrogen and carbon dioxide adsorption. The conclusions obtained from this research are as follows.

(1) Oil expulsion efficiency can strongly affect organic gas generation and nanopore development in highly mature shales. As exemplified here, bitumen remained in shales with low oil-expulsion efficiency, which accounts for 60% of the TOC in the shales, contributes 43%–53% of C_1 as well as 70%–98% of C_2–C_5 gas yields, and 52%–72% of pore (D < 10 nm) volumes at high maturity.

(2) The evolution of micropores and fine mesopores in highly mature shales can be divided into two stages: Stage I, corresponding to wet gas generation (EasyRo 1.2%–2.4%); and Stage II, corresponding to dry gas generation (EasyRo 2.4%–4.5%). For shales with low oil expulsion efficiency, pore evolution increases rapidly in Stage I, whereas slowly in Stage II, and such difference between two stages may be attributed to the changes of the OM's mechanical properties, as it evolves from flexible to brittle. Comparatively, for shales with high oil expulsion efficiency, the evolution grows slightly in Stage I, not as fast as shales with low efficiency, and decays in Stage II. The differences of pore evolutions between these two suites are attributed to the contribution of bitumen. However, the evolution of medium–coarse mesopores and macropores (>10 nm) remains flat at high maturation.

(3) Despite the capacity of bitumen for pore generation, its presence may also fill the intra- and intergranular spaces among kerogen and minerals. The effect of pore blocking by bitumen outweighs its pore generation capacity on micropores, whereas these two effects counteract each other on fine mesopores.

(4) For shales at the gas generating stage, high reservoir pressure with increasing burial depth can promote the development of micropores and fine mesopores, whereas it has complicated effects on the evolution of medium–coarse mesopores and macropores.

Acknowledgements

This work was financially supported by Special Fund for Strategic Priority Research Program of the Chinese Academy of Sciences (Class B) (Grant No. XDB10010500) and Natural Science Foundation of China (Grant Number: 41621062). We are grateful to Section Editor Dr. Qinhong Hu and anonymous reviewer for their instructive comments and suggestions that significantly help clarify this manuscript. This is contribution No. IS-2398 from GIGCAS.

Appendix A. Supplementary data

Supplementary data related to this article can be found at http://dx.doi.org/10.1016/j.marpetgeo.2017.06.012.

References

Barrett, E.P., Joyner, L.G., Halenda, P.P., 2014. The determination of pore volume and area distributions in porous substances. I. Computations from nitrogen isotherms. J. Manag. Eng. 24 (4), 207–216.
Bernard, S., Horsfield, B., Schulz, H.M., Wirth, R., Schreiber, A., Sherwood, N., 2012a. Geochemical evolution of organic-rich shales with increasing maturity: a STXM and TEM study of the Posidonia Shale (Lower Toarcian, northern Germany). Mar. Pet. Geol. 31 (1), 70–89.
Bernard, S., Wirth, R., Schreiber, A., Schulz, H., Horsfield, B., 2012b. formation of nanoporous pyrobitumen residues during maturation of the barnett shale (fort worth basin). Int. J. Coal Geol. 103, 3–11.
Chalmers, G.R., Bustin, R.M., Power, I.M., 2012. Characterization of gas shale pore systems by porosimetry, pycnometry, surface area, and field emission scanning electron microscopy/transmission electron microscopy image analyses: examples from the Barnett, Woodford, Haynesville, Marcellus, and Doig units. AAPG Bull. 96 (6), 1099–1119.
Chalmers, G.R.L., Bustin, R.M., 2007. The organic matter distribution and methane capacity of the Lower Cretaceous strata of Northeastern British Columbia, Canada. Int. J. Coal Geol. 70 (1), 223–239.
Chao, Y., Zhang, J., Xuan, T., 2013. Microscopic pore types and its impact on the storage and permeability of continental shale gas,Ordos Basin. Earth Sci. Front. 20 (4), 240–250.
Chen, J., Xiao, X., 2014. Evolution of nanoporosity in organic-rich shales during thermal maturation. Fuel 129, 173–181.
Chen, S., Zhu, Y., Wang, H., Liu, H., Wei, W., Fang, J., 2011. Shale gas reservoir characterisation: a typical case in the southern Sichuan Basin of China. Energy 36 (11), 6609–6616.
Curtis, M.E., Cardott, B.J., Sondergeld, C.H., Rai, C.S., 2012. Development of organic porosity in the Woodford Shale with increasing thermal maturity. Int. J. Coal Geol. 103, 26–31.
Dong, D., Gao, S., Huang, J., Guan, Q., Wang, S., Wang, Y., 2015. A discussion on the shale gas exploration & development prospect in the Sichuan Basin. Nat. Gas Ind. 34 (12), 1–15.
Emmanuel, S., Eliyahu, M., Day-Stirrat, R.J., Hofmann, R., Macaulay, C.I., 2016. Impact of thermal maturation on nano-scale elastic properties of organic matter in shales. Mar. Pet. Geol. 70, 175–184.
Fitzgerald, D., 1956. The kinetics of coal carbonization in the plastic state. Trans. Faraday Soc. 52 (2), 84–90.
Ghanizadeh, A., Amann-Hildenbrand, A., Gasparik, M., Gensterblum, Y., Krooss, B.M., Littke, R., 2014. Experimental study of fluid transport processes in the matrix system of the European organic-rich shales: II. Posidonia Shale (Lower Toarcian, northern Germany). Int. J. Coal Geol. 123 (2), 20–33.
Hao, F., Zou, H., Lu, Y., 2013. Mechanisms of shale gas storage: implications for shale gas exploration in China. AAPG Bull. 97 (8), 1325–1346.

Hua, T., 2012. Determination of organic-rich shale pore features by mercury injection and gas adsorption methods. Acta Pet. Sin. 33 (3), 419–427.
Huang, W.L., 1996. Experimental study of vitrinite maturation: effects of temperature, time, pressure, water, and hydrogen index. Org. Geochem. 24 (2), 233–241.
Jarvie, D.M., 2012. Shale resource systems for oil and gas: Part 1—shale-gas resource systems. AAPG Mem. 97, 89–119.
Jarvie, D.M., Hill, R.J., Ruble, T.E., Pollastro, R.M., 2007. Unconventional shale-gas systems: the Mississippian Barnett Shale of north-central Texas as one model for thermogenic shale-gas assessment. AAPG Bull. 91 (4), 475–499.
Jia, W., Wang, Q., Liu, J., Peng, P., Li, B., Lu, J., 2014. The effect of oil expulsion or retention on further thermal degradation of kerogen at the high maturity stage: a pyrolysis study of type II kerogen from Pingliang shale, China. Org. Geochem. 71, 17–29.
Klaver, J., Desbois, G., Littke, R., Urai, J.L., 2015. BIB-SEM characterization of pore space morphology and distribution in postmature to overmature samples from the Haynesville and Bossier Shales. Mar. Pet. Geol. 59, 451–466.
Knauss, K.G., Copenhaver, S.A., Braun, R.L., Burnham, A.K., 1997. Hydrous pyrolysis of New Albany and Phosphoria Shales: production kinetics of carboxylic acids and light hydrocarbons and interactions between the inorganic and organic chemical systems. Org. Geochem. 27 (7–8), 477–496.
Liu, S., Yong-Sheng, M.A., Cai, X., Guo-Sheng, X., Wang, G., Yong, Z., Wei, S., Yuan, H., 2009. Characteristic and accumulation process of the natural gas from sinian to lower paleozoic in Sichuan Basin,China. J. Chengdu Univ. Technol. 36 (4), 345–354.
Long, P., Zhang, J., Li, Y., Tang, X., Cheng, L., Liu, Z., Han, S., 2012. Reservoir-forming conditions and strategic select favorable area of shale gas in the Lower Paleozoic of Chongqing and its adjacent areas. Earth Sci. Front. 19 (02), 221–233.
Loucks, R.G., Reed, R.M., Ruppel, S.C., Jarvie, D.M., 2009. Morphology, genesis, and distribution of nanometer-scale pores in siliceous mudstones of the mississippian barnett shale. J. Sediment. Res. 79 (12), 848–861.
Lu, J., 1990. The modelling experiment of coal-generated hydrocarbons. In: Fu, J., Liu, D., Sheng, G. (Eds.), Geochemistry of Coal-generated Hydrocarbons. Science Press, Beijing, China, pp. 40–46.
Ma, Y., Zhang, S., Guo, T., Zhu, G., Cai, X., Li, M., 2008. Petroleum geology of the Puguang sour gas field in the Sichuan Basin, SW China. Mar. Pet. Geol. 25 (4–5), 357–370.
Mastalerz, M., Schimmelmann, A., Drobniak, A., Chen, Y., 2013. Porosity of Devonian and Mississippian New Albany Shale across a maturation gradient: insights from organic petrology, gas adsorption, and mercury intrusion. AAPG Bull. 97 (10), 1621–1643.
Mathia, E.J., Bowen, L., Thomas, K.M., Aplin, A.C., 2016. Evolution of porosity and pore types in organic-rich, calcareous, Lower Toarcian Posidonia Shale. Mar. Pet. Geol. 75, 117–139.
Milliken, K.L., Rudnicki, M., Awwiller, D.N., Zhang, T., 2013. Organic matter–hosted pore system, marcellus formation (Devonian), Pennsylvania. AAPG Bull. 97 (2), 177–200.
Neaman, A., Pelletier, M., Villieras, F., 2003. The effects of exchanged cation, compression, heating and hydration on textural properties of bulk bentonite and its corresponding purified montmorillonite. Appl. Clay Sci. 22 (4), 153–168.
Noyan, H., Önal, M., Sarikaya, Y., 2006. The effect of heating on the surface area, porosity and surface acidity of a bentonite. Clays Clay Minerals 54 (3), 375–381.
Pan, C., Jiang, L., Liu, J., Zhang, S., Zhu, G., 2010. The effects of calcite and montmorillonite on oil cracking in confined pyrolysis experiments. Org. Geochem. 41 (7), 611–626.
Pan, C., Jiang, L., Liu, J., Zhang, S., Zhu, G., 2012. The effects of pyrobitumen on oil cracking in confined pyrolysis experiments. Org. Geochem. 45, 29–47.
Ross, D.J.K., Marc Bustin, R., 2009. The importance of shale composition and pore structure upon gas storage potential of shale gas reservoirs. Mar. Pet. Geol. 26 (6), 916–927.
Shi, M., Yu, B., Xue, Z., Wu, J., Yuan, Y., 2015. Pore characteristics of organic-rich shales with high thermal maturity: a case study of the Longmaxi gas shale reservoirs from well Yuye-1 in southeastern Chongqing, China. J. Nat. Gas Sci. Eng. 26 (4), 948–959.
Shuai, Y., Peng, P., Zou, Y., 2006. Influence of pressure on stable carbon isotope ratio and production yield of coal-derived methane. Fuel 85 (5–6), 860–866.
Sun, L., Tuo, J., Zhang, M., Wu, C., Wang, Z., Zheng, Y., 2015. Formation and development of the pore structure in Chang 7 member oil-shale from Ordos Basin during organic matter evolution induced by hydrous pyrolysis. Fuel 158, 549–557.
Sun, W., Liu, S., Ran, B., Wang, S., Yue-Hao, Y.E., Luo, C., 2012. General situation and prospect evaluation of the shale gas in Niutitang Formation of Sichuan Basin and its surrounding areas. J. Chengdu Univ. Technol. 39 (2), 170–175.
Sweeney, J.J., Burnham, A.K., 1990. Evaluation of a simple model of vitrinite reflectance based on Chemical kinetics. Aapg Bull. 74 (10), 1559–1570.
Tan, J., Horsfield, B., Fink, R., Krooss, B., Schulz, H.M., Rybacki, E., Zhang, J., Boreham, C.J., Graas, G.V., Tocher, B.A., 2014. Shale gas potential of the major marine shale formations in the upper Yangtze platform, south China, Part III: mineralogical, lithofacial, petrophysical, and rock mechanical properties. Energ. Fuel. 28 (4), 2322–2342.
Tang, X., Zhang, J., Jin, Z., Xiong, J., Lin, L., Yu, Y., Han, S., 2015. Experimental investigation of thermal maturation on shale reservoir properties from hydrous pyrolysis of Chang 7 shale, Ordos Basin. Mar. Pet. Geol. 64, 165–172.
Tao, W., Zou, Y.R., Carr, A., Liu, J., Peng, P.A., 2010. Study of the influence of pressure on enhanced gaseous hydrocarbon yield under high pressure–high temperature coal pyrolysis. Fuel 89 (11), 3590–3597.
Thommes, M., Kaneko, K., Neimark, A.V., Olivier, J.P., Rodriguezreinoso, F., Rouquerol, J., Sing, K.S.W., 2015. Physisorption of gases, with special reference to the evaluation of surface area and pore size distribution (IUPAC Technical Report). Pure Appl. Chem. 87 (9), 25.
Tian, H., Pan, L., Zhang, T., Xiao, X., Meng, Z., Huang, B., 2015. Pore characterization of organic-rich lower cambrian shales in qiannan depression of Guizhou Province, southwestern China. Mar. Pet. Geol. 62, 28–43.
Tuo, J., Wu, C., Zhang, M., 2016. Organic matter properties and shale gas potential of Paleozoic shales in Sichuan Basin, China. J. Nat. Gas Sci. Eng. 28 (57), 434–446.
Uguna, C.N., Carr, A.D., Snape, C.E., Meredith, W., 2014. High pressure water pyrolysis of coal to evaluate the role of pressure on hydrocarbon generation and source rock maturation at high maturities under geological conditions. Org. Geochem. 78 (5103), 44–51.
Valenza, J.J., Drenzek, N., Marques, F., Pagels, M., Mastalerz, M., 2013. Geochemical controls on shale microstructure. Geology 41 (5), 611–614.
Wang, Y., Dong, D., Cheng, X., Huang, J., Wang, S., Wang, S., 2014. Electric property evidences of carbonification of organic matters in marine shales and its geologic significance: a case study of the Lower Cambrian Qiongzhusi Shale in the southern Sichuan Basin. Nat. Gas Ind. B 1 (4), 129–136.
Wei, M., Zhang, L., Xiong, Y., Li, J., Peng, P., 2016. Nanopore structure characterization for organic-rich shale using the non-local-density functional theory by a combination of N2 and CO2 adsorption. Microporous Mesoporous Mater. 227, 88–94.
Xiao, X.M., Wang, M.L., Wei, Q., Tian, H., Pan, L., Teng-Fei, L.I., 2015. Evaluation of lower paleozoic shale with shale gas prospect in south China. Nat. Gas Geosci. 26 (8), 1433–1445.
Xiao, X.M., Song, Z.G., Zhu, Y.M., Hui, T., Yin, H.W., 2013. Summary of shale gas research in North American and revelations to shale gas exploration of Lower Paleozoic strata in China south area. J. China Coal Soc. 38 (5), 721–727(7).
Xiao, X.M., Tian, H., Liu, D.H., Liu, Z.F., 2012. Evaluation of Deep Burial Source Rocks and Their Natural Gas Potentials in Sichuan Basin. Research Program of China (Project No. 2011ZX05008-002-40), Internal Report. Guangzhou Institute of Geochemistry of Chinese Academy of Sciences.
Xiong, Y., Zhang, L., Chen, Y., Wang, X., Li, Y., Wei, M., Jiang, W., Lei, R., 2016. The origin and evolution of thermogenic gases in organic-rich marine shales. J. Pet. Sci. Eng. 143, 8–13.
Yang, F., Ning, Z., Wang, Q., Zhang, R., Krooss, B.M., 2016. Pore structure characteristics of lower Silurian shales in the southern Sichuan Basin, China: insights to pore development and gas storage mechanism. Int. J. Coal Geol. 156, 12–24.
Yang, W., Zhu, Y., Chen, S., Wu, L., 2014. Characteristics of the nanoscale pore structure in northwestern hunan shale gas reservoirs using field emission scanning electron microscopy, high-pressure mercury intrusion, and gas adsorption. Energy Fuels 28 (2), 945–955.
Zhang, J.C., Nie, H.K., Bo, X.U., Jiang, S.L., Zhang, P.X., Wang, Z.Y., 2008. Geological condition of shale gas accumulation in Sichuan Basin. Nat. Gas Ind. 28 (2), 151–156.
Zou, C., Dong, D., Wang, S., Li, J., Li, X., Wang, Y., Li, D., Cheng, K., 2010. Geological characteristics and resource potential of shale gas in China. Pet. Explor. Dev. 37 (6), 641–653.
Zou, C., Dong, D., Wang, Y., Li, X., Huang, J., Wang, S., Guan, Q., Zhang, C., Wang, H., Liu, H., 2015. Shale gas in China: characteristics, challenges and prospects (II). Pet. Explor. Dev. 42 (6), 753–767.